Geochemical evidence for arsenic cycling in living microbialites of a High Altitude Andean Lake (Laguna Diamante, Argentina)

Maria Sancho-Tomas, Andrea Somogyi, K. Medjoubi, Antoine Bergamaschi, Pieter T. Visscher, Alexander van Driessche, Emmanuelle Gerard, María Farias, Pascal Philippot

HAL Id: hal-02912566

https://hal.umontpellier.fr/hal-02912566v1

Submitted on 15 Dec 2020

Geochemical evidence for arsenic cycling in living microbialites of a High Altitude Andean Lake (Laguna Diamante, Argentina)

María Sancho-Tomás (a),*, Andréa Somogyi (b), Kadda Medjoubi (b), Antoine Bergamaschi (b), Pieter T. Visscher (c and d), Alexander E. S. van Driessche (e), Emmanuelle Gérard (a), María E. Farias (f), Manuel Contreras (g) and Pascal Philippot (a and h)

a Institut de Physique du Globe de Paris, Paris, France

b Synchrotron Soleil, Saint-Aubin, France

c UMR CNRS 6282 Biogéosciences, Université de Bourgogne Franche-Comté, Dijon, France

d Department of Marine Sciences, University of Connecticut, Groton, USA

e Université Grenoble Alpes, Université Savoie Mont Blanc, CNRS, IRD, IFSTTAR, ISTerre, Grenoble, France

f LIMLA - PROIMI - CONICET, San Miguel de Tucumán, Argentina

g Centro Ecologia Aplicada, 2-2741872 Santiago, Chile

h CNRS-UMR 5243, Université de Montpellier, Montpellier, France

Geochemical evidence for arsenic cycling in living microbialites of a High

Altitude Andean Lake (Laguna Diamante, Argentina)

ABSTRACT

Arsenic is best known as an environmental toxin, but this element could also serve as a metabolic energy source to certain microorganisms. Moreover, As cycling may have driven microbial life on early Earth prior to oxygenation of the atmosphere. Still, little is known about the arsenic cycling processes occurring in the presence of microorganisms and the possible traces that could be preserved in the rock record. To advance our understanding of this we studied the geochemical proxies of microbial As metabolism in living microbialites from Laguna Diamante, a likely Precambrian ecosystem analogue (Catamarca, Argentina). In this study, we show that the coexistence of As(III) and As(V) strongly supports the presence of active microbially arsenic cycling in these microbialites. In addition, we propose a model by which arsenic metabolic processes can be preserved and interpreted as biosignatures in modern systems as well as in the rock record.

INTRODUCTION

Although arsenic is mainly considered to be highly toxic to organisms in all three domains of life, many microorganisms have evolved to tolerate relatively high concentrations of this metalloid and some even benefit from it as a source of energy for their growth (Sun & Lloyd, 2010). There are several lines of geological evidence, which indicate that As may have played a prominent role on early Earth. For instance, after the early accretionary phase of the Earth, after it had cooled and differentiated, sulfur and chalcophilic elements (e.g., As) were significantly enriched within the mantle and the core relative to the crust due to the sinking of the denser metal(loid)-sulfides. Due to widespread volcanism and geothermal activity characteristic of Archean Earth, As would have been brought back to the Earth's surface (e.g. Cabral & Beaudoin, 2007; Witt-Eickschen *et al.,* 2009). In addition, like many modern hot springs, abundant hydrothermally-influenced systems on the Precambrian Earth presumably contained high concentrations of reduced As(III). Hence, it is likely that prior to the rise of atmospheric oxygen about 2.5 Ga ago, substantial amounts of reduced As were present in the oceans thereby posing a biochemical challenge (but also a potential opportunity) for early emergent life. This is certainly supported by biomolecular studies which have demonstrated that the arsenite oxidase enzyme *Aro* has a deeply-rooted origin that predates the divergence of Archaea and Bacteria from the last universal common ancestor (Lebrun et al., 2003; Duval et al., 2008). Nonetheless, the role of arsenic cycling in early Earth ecosystems is still not well understood. This could be improved by studying the arsenic mechanisms in microorganisms living today in high arsenic environments and severe conditions.

As cycling in modern sediments and bacteria cultures, implying bacteria mediated As(V) reduction and As(III) oxidation, has been reported for extreme environments, such as the alkaline hypersaline waters of Mono and Searles Lakes, California (Oremland *et al.*, 2005; van Lis *et al.*, 2013; Munoz *et al.*, 2018). Evidence for a complete As cycle have been detected in High-altitude Andean Lakes such as La Brava, Diamante and Socompa Lakes (Farías *et al.*, 2013; Kurth *et al.*, 2017). Sequences for arsenite oxidases and respiratory arsenate reductase have been identified in haloarchaea from

Diamante and Tebenchique Lakes, suggesting that in addition to detoxification processes, these microbes could also use arsenic redox reactions to obtain energy (Lara *et al.*, 2012; Rascovan *et al.*, 2016; Ordoñez *et al.*, 2018). However, very few biogeochemical data supporting this claim have been reported so far.

 Recently, Chi Fru and coworkers indicated that the concentration of As(V) increased rapidly during the Great Oxidation Event, which may have enabled the expansion of a global As cycle (Chi Fru *et al.*, 2019). In a previous study, Sforna et al. reported the discovery of 2.7-billion-year-old stromatolites from Tumbiana, in which fossilized microorganisms and biogenic $CaCO_3$ minerals were associated with high concentrations of As (Sforna *et al.*, 2014). Based on hierarchical length-scale information of the element distribution and inter-element correlations, Sforna and colleagues argued that Tumbiana stromatolites were formed by microbial mats thriving in an anoxic, salt-saturated lake setting, and, importantly, in which As(III) oxidation and As(V) reduction metabolic pathways were taking place (Sforna *et al.*, 2014).

Calculations have shown that arsenic cycling may play a role in microbialite formation (i.e. $CaCO_3$ precipitation) (Visscher, 2014). Microbially-mediated $CaCO_3$ precipitation has two components. Firstly, the metabolism of the microbial community influences the geochemical environment through which the speciation of calcium and carbonate ions is altered (i.e. change the alkalinity). Secondly, the functional groups in the exopolymeric substance (EPS) matrix influences the mineral product formation through cation binding and successive release by providing preferential mineral nucleation sites (Dupraz & Visscher, 2005). Other elements (e.g. metal(loid)s) may be incorporated in $CaCO_3$ solids. For example, calcite, the most stable polymorph of $CaCO_3$, is capable of retaining trace elements via adsorption (surface) reactions as well as through co-precipitation reactions (Alexandratos *et al.*, 2007). Furthermore, certain types of EPS components (e.g. agarose or the organic matrix extracted from marine organisms) can interfere the growth of calcite crystals (Li *et al.*, 2009; Rae Cho *et al.*, 2016). Consequently, physicochemical incorporation of metal(loid)s in polymers (such as EPS) is a viable mechanism by which other trace metal(loid)s including As can become incorporated in crystals, specifically calcite (Huerta-Diaz *et al.*, 2012; Sforna *et al.*, 2017). Arsenic could be also incorporate in the calcite lattice by the substitution of a CO_3^{2-} and AsO_3^{3-} as it has been observed in the As-bearing travertine rocks (Bardelli *et al.*, 2011). Through these different mechanisms, As can be retained and preserved in the rock record. However, to date, the link between $CaCO_3$ biomineralization and As has not been clarified.

The goal of this study is to identify geochemical proxies of As-based metabolisms and its preservation in living microbialites of Laguna Diamante, which are considered to be likely analogues of early Earth. To achieve this, we have characterized at multiple length scales the geochemical imprint of microbially-mediated arsenic cycling in present day samples, from superficial, biologically active, organic-rich zone to the internal carbonate-rich area in advanced stages of lithification. We combined powder X-ray diffraction (PXRD), scanning electron microscopy with energy dispersive X-ray analysis (SEM-EDX) and Confocal Laser Scanning Microscopy (CLSM) with synchrotron scanning techniques, including X-ray micro-fluorescence (μXRF), X-ray Absorption Near Edge Structure (XANES) imaging and punctual XANES analyses (Somogyi *et al.*, 2015).

MATERIALS AND METHODS

Sample collection

The hypersaline shallow Laguna Diamante is located in the caldera of the Galán Volcano in Catamarca, Argentina, at approximately 4590 meters above sea level (Fig. 1a). Samples were in January 2015 from the shallow part of the Laguna Diamante. Round to oval-shaped rocks, around 1cm in diameter were partially exposed to the atmosphere but during daily high-wind events were completely submersed during part of the day. The rocks were covered by semi-continuous purple layer with building-up tubular-shaped microbialitic buildups (Fig. 1b and c). The samples were immediately wrapped in PVDC plastic, transported to the lab in plastic containers and stored in the dark at 4 °C.

Water chemistry

The pH and the temperature were measured using a Metter-Toledo GoFive handheld pH/temperature probe. The conductivity and the salinity were determined with a Fisher Accumet AP75 handheld conductivity/temperature probe. Three replicas of water samples were taken ca. 5 cm above the mat and stored in glass vials (4-ml vials either under in situ pH conditions, acidified for analysis of major ions or fixed in 1.25 mM EDTA 87 mM acetic acid to determine the arsenic concentration). The water samples were kept refrigerated while being transported to the laboratory. Major cation (NH_4^+, K^+, Mg^{2+} and Ca^{2+}) and anion (SO_4^{2-} and NO_3^-) concentrations were determined by ion chromatography (Dionex ICS 3000) (Pace *et al.*, 2018). The physicochemical composition of the water, given in Table 1, represents the average composition of the three water samples.

Mineralogical and elemental analysis

X-ray diffraction (PXRD). The mineral composition was determined by powder X-ray diffraction in a chamber with controlled temperature and humidity. Finely grounded powder of fresh samples were analyzed using a Panalytical X'per MPD diffractometer with copper anode (Cu Ka radiation). The diffraction patterns were collected from 5 to 80º (2θ) at 100% humidity and decreasing humidity (until 50% relative humidity). The patterns thus obtained were analyzed employing the program XPowder (Martin, 2004) with the ICDD-PDF2 database. The results are shown in Fig. SI1.

Microscopy SEM-EDX. The thin section of Fig. 3a was observed under vacuum using a Zeiss EVO SEM equipped with an Energy Dispersive Spectrometer (Bruker) using a voltage of 15 keV and a current beam of 2 nA (Fig. 2). Spectra were analyzed using the software Quantax 200 (Bruker).

Major and trace element analysis. The major and trace element composition of the portion of microbialite investigated using synchrotron X-ray microfluorescence were analyzed at the "Services d'Analyses des roches et des Minéraux" (SARM) du Centre de Recherches Pétrographiques et Géochimiques de Nancy, France (Table 2). Major and trace elements were measured by ICP-OES and ICP-MS, respectively. The uncertainties are 5% for concentrations greater than 10 ppm and 15% for concentrations between 10 and 1 ppm (See Carignan *et al.*, (2001) for a detail description of the experimental protocols use at SARM for major and trace element analyses).

Confocal laser scanning microscopy analysis. The thin section of Fig. 3a was examined using a FluoView FV1000 CLSM with spectral resolution of 2 nm and spatial resolution of 0.2 m *(*Olympus

Tokyo, Japan). An additional section of the fresh microbialite was also inspected. For examination of the later, an oil immersion objective UPLSAPO 60XO (Olympus; 60 magnification, numerical aperture 1.35) was used. Fluorescence stack images for both samples were obtained with a concomitant excitation at wavelengths of 405, 488 and 543 nm by collecting the emitted fluorescence between 425-475, 500-530 and 560-660 nm. Fluorescence spectra were acquired by collecting the emitted fluorescence between 435 and 796 nm, with bandwidth analyses of 10 nm and step size of 5 nm. The images were visualized and processed using the F10-ASW FLUOVIEW software (Olympus) (Fig. S4). The samples were investigated following the protocol described by Gérard *et al.*, (2013).

Synchrotron analysis

For synchrotron analysis, microbialites were progressively dehydrated in a series of ethanol baths (30%, 50%, 70%, 90% and 100%) and then gradually impregnated with hard grade LR-white resin (for details on the protocol, see Gérard *et al.*, (2013)). This resin has a strong resistance to prolonged light exposure inherent to imaging and is free of metallic impurities. Petrographic thin sections were cut with a diamond wire saw and polished down to homogenous thickness of ~100 μm (Fig. 3a). All synchrotron analyses were performed at the Nanoscopium beamline (SOLEIL synchrotron facility, France)(Somogyi *et al.*, 2015). The sample was raster scanned in a focused X-ray beam while measuring the emitted secondary radiation and/or the transmitted beam at each position. The spatial resolution is determined by the beam-size and the experimental conditions and was between μm and 500 nanometers during the recent measurements.

Synchrotron radiation X-ray micro-Fluorescence (SR-μXRF). A monochromatic incident X-ray beam was focused into a 300 x 300 nm^2 FWHM spot (Full Width at Half Maximum) at the sample position by using Kirckpatrick-Baez (KB) mirrors. The incident beam energy, 12 keV, was chosen by a double-crystal Si(111) monochromator, just above the As K-edge for XRF imaging. At this energy, the measured photon flux in the 300 x 300 nm^2-sized focused beam was ~2×10^{10} photons/s. The sample was mounted onto a 3-axis sample positioning stage. The X-ray fluorescence radiation emitted by the sample was recorded by two identical silicon drift detectors of 50 mm^2 active surfaces (KETEK H50, KETEK GmbH) used with XMAP (XIA LLC) fast digital multichannel analyzer cards. The detectors were placed at backscattering geometry at ~100° compared to the incoming X-ray beam (at ~10° compared to the sample surface) (Somogyi *et al.*, 2015). Elemental distribution maps (Fig. 3c-e and SI2) were reconstructed from the XRF spectra by using preselected spectral regions of interest (ROIs) and summing the intensities measured by the two detectors (Bergamaschi *et al.*, 2016). A deconvolution procedure using PyMCA (Solé *et al.*, 2007) was applied in case of overlapping X-ray peaks. The transmitted X-ray beam was recorded by a 300 μm-thick Si diode placed behind the sample, providing information about the morphology of the sample.

2D elemental distribution and transmission contrast maps were measured. In a first step, a large field of view (H x V = 720 μm x 700 μm) 1 μm x 1 μm resolution map was collected with 10 ms dwell time per point (Fig. 3b-e); for the second step, a medium field of view (H x V = 450 μm x 170 μm) 0.5 μm x 0. 5 μm resolution map was measured with 15 ms dwell time per point (Fig. SI2). In order to compare the elemental distribution maps measured with different dwell times, the intensity maps were normalized by the incident X-ray intensities (I_0) recorded for each pixel. Further data treatment was performed in Matlab.

X-ray absorption near edge structure (XANES). Seven different pellets and mineral standards were used for calibrating the XANES analysis of arsenic. These include: arsenopyrite (AsFeS), orpiment

(As$_2$S$_3$), fetiasite (As(III)-fet, (Fe(II,III)Ti)$_3$(As(III)$_2$O$_5$)O$_2$; As$_2$O$_3$ pellet (Sigma-Aldrich), arsenobetaine (Asbet, C$_5$H$_{11}$AsO$_2$), legrandit (As(V)-leg, Zn$_2$(As(V)O$_4$)(OH)·(H$_2$O)) and As$_2$O$_5$ pellet (Sigma-Aldrich).

XANES spectra were collected by scanning the energy at 0.5 eV steps around the K-edge of As in X-ray fluorescence and transmission modes. The beam energy was calibrated by defining the edge position of the As$_2$O$_5$ standard at 11.8745 keV. The inflections points of the As K-edge XANES spectrum remained stable within 0.5 eV during this measurement period. To ensure the absence of photo-oxidation/reduction during synchrotron measurements, several As-XANES spectra were collected successively as a function of time in some selected points of the sample. No changes in these successive XANES spectra have been detected.

In order to determine the spatial variation of arsenic speciation in the sample, several "characteristics" X-ray energies were defined for XANES mapping, which correspond to the white lines of the XANES spectra of the FeAsS, As$_2$S$_3$, As$_2$O$_3$, Asbet and As$_2$O$_5$ standards (Fig. SI3). In addition, three energy points were selected, corresponding to the pre- and far away As K-edge, and a medium energy point between Asbet and As$_2$O$_5$. The resulting excitation energies (11.8653, 11.8684, 11.8696, 11.8714, 11.8727, 11.8745 and 11.8819 keV) allowed tracking the variations of arsenic speciation variation in the sample. For each incident X-ray energy, a XRF map was obtained, representing a total of 7 X-ray maps for the selected zone of measurement. The obtained As speciation maps were treated with Matlab software. Only As$_2$O$_3$, [As(III)], and As$_2$O$_5$, [As(V)], dominant regions are shown here for clarity (Fig. 5). Micro-XANES measurements were also performed in several spots of the mat sample.

Principal Component Analysis (PCA) and clustering. The elemental intensities obtained from the XRF spectra were further analyzed by Principal Component Analysis (PCA) for data reduction and to identify quantitatively the dominant modes of metal associations and spatial distributions. The principal components are linear combinations of the original elemental intensities, along which the variation in the data is maximal. Since PCA is designed to identify directions with the largest variation, it is not adapted for the identification of groups describing small sample variance. In the present case, the method was well-suited for discarding several variables and obtaining a final multivariate analysis with the chemical elements most linked with arsenic (As, Ca and Fe). The principal components for the As, Ca and Fe stack of the higher resolution maps were determined and cluster analysis was performed on the dataset based on the components with the higher contribution of arsenic (Fig. 4b). Cluster analyses provides an "assumption-free" analysis of the distribution of chemical components in the sample, by classifying pixels according to their spectral similarity (Etschmann *et al.*, 2014). Scatterplots were derived from the clustering analysis (Fig. 4c).

The ratios of As(V)/As(III) and As/Ca were calculated by dividing the As(V) intensity counts by the As(III) counts and the As intensity counts by the Ca counts, respectively (Fig. 4d). The ratios were calculated for the different clusters areas, indicated in different colors in figure 4b.

RESULTS

Microbialite environment

Laguna Diamante is located inside the Galan Volcano caldera (Fig. 1a), in Catamarca, Argentina (26°00'51.04'S, 67°01'46.42'O). This is one of the largest uncovered volcano calderas of the world, measuring 34 km by 20 km, and is surrounded by mountain ranges > 6000 meters in altitude. Galan

Volcano reaches 5912 m above sea level and hosted extensive volcanic activity from the upper Miocene to the Pleistocene (7 to 4 Ma) (Soler *et al.*, 2007; Ruggieri *et al.*, 2010). This environment is strongly influenced by hydrothermal sources, large temperature fluctuations (water temperature fluctuates daily from 1.2ºC to 21.2ºC, strong UV radiations (maximum UV-AB reaches ca. 71.3 Wm^{2}), hypersaline, alkaline (pH=9.1-10.7) water conditions and a high arsenic concentration (2.27 ± 0.88 mM).

Microbialite characterization

Laguna Diamante microbialites occur as partially submerged calcareous formations, showing tube-forming thrombolitic structures of several centimeters in size (insert in Fig. 1c). The microbialite investigated in this study was sampled near the shoreline and intermittently exposed to air. The horizontal cross section of the Laguna Diamante microbialites revealed a concentric layered structure with three distinct zones: an external, pink crystalline surface; a medium, organic-rich part, composed of two dominant colored layers, purple and green, and an internal part primarily composed of clotted carbonate (Fig. 1d).

PXRD analyses showed that calcite is the main phase and gaylussite (Na$_2$Ca(CO$_3$)$_2$ - 5 H$_2$O), phyllosilicates and quartz occur as secondary phases (Fig. S1). Gaylussite, which corresponds to the pink layer, covers the tubular structure of the microbialites and is likely formed through efflorescence from the alkaline (9-10 pH) lacustrine water, similar to those found in lake Magadi, in Kenia (pH>9.5, Jones *et al.*, (1977)) and Mono Lake, in USA (pH>9.5(Bischoff *et al.*, 1991)). Importantly, no traces of this mineral are found inside the microbialites. The internal part of the microbialite is mainly composed of calcite. SEM images showed that calcite typically appeared either as large >50 µm (Fig. 2a), or small aggregates, ~3-5 µm (Fig. 2b). Secondary phases detected included phyllosilicates and quartz that were most likely derived from weathering of the volcanic rocks, which form the local basement of Laguna Diamante. Halite was detected only when the humidity in the PXRD chamber was decreased and halite precipitated due to evaporation of the residual water trapped in the fresh sample (Fig. SI1).

Intercorrelation of arsenic and other elements

In order to determine the distribution of arsenic within the microbialite, we performed X-ray synchrotron radiation analyses in a selected area of the sample that included both organic-rich and carbonate-rich regions (the studied area is marked with an orientative black box in Fig. 1d and the exact measured area is shown in Fig. 3a). The selected area showed contrasted organic-rich (left side) and carbonate-rich (right side) regions (Fig. 3a). This can be better seen in the transmission image (Fig. 3b), where the low transmission region in the upper-right part of the sample is enriched in Ca (Fig 3d), attributed to carbonate minerals. This Ca-rich region appears linked to As (Fig. 3c). This is in contrast with the organic-rich region, indicated by the high transmission signal (center-left side of Fig. 3b). In this organic-rich zone, As and Ca show a heterogeneous distribution characterized by disseminated small (< 10 µm) hotspots (Fig. 3b and c). Complementary ICP-MS analyses highlighted the presence of Fe. Iron occurred as heterogeneously distributed hotspots in the organic-rich region (Fig. 3d). Other relatively abundant low Z elements detected by ICP-MS such as Na and Mg, or high Z elements, such as Sr and Rb, could not be detected with the experimental protocol used at Nanoscopium (see Mat&Met).

In order to better understand the chemical behavior of As in the organic-rich zone, the area marked by a yellow frame in Fig. 3c was analyzed with a 0.5 x 0.5 µm spatial resolution mapping, using 15

ms/pixel integration time (Fig. SI2, Fig. 4). The RGB image of As (green), Ca (red) and Fe (blue) of Fig. 4a shows that As occurs as a disseminated compound in irregular globular domains about 3 to 5 μm in diameter (these domains will be referred as globules or globular distribution in the following text)). These globules are devoid, or contain only minor amounts of Fe and Ca. Noteworthy, the top right corner of Fig. 4a shows that As and Ca are correlated in the carbonate-rich region.

In order to gain detailed insight on the spatial distribution and the degree of co-localization of As with Ca and Fe, clustering and scatter plots were combined with PCA (Fig. 4b and c). The obtained clustering image highlighted three types of As distribution: (i) a globular distribution of As with minor contribution of Ca and Fe (labeled {As1} and marked in green), (ii) areas attributed to carbonate (labeled {As2} and marked in dark red), with a high correlation between As and Ca (indicated by the 2D plot), and (iii) disseminated As showing a diffuse pattern in the RGB image (Fig. 4a). These are represented by the light blue pixels of {As3}, where Fe and Ca are both correlated with As. The distribution labeled {As4} and marked in orange correspond to Ca, with no As or Fe correlation. In addition, the calculated As/Ca ratio for the three major distributions of arsenic showed that the irregular globules {As1} contain the highest As/Ca ratio, while the carbonate area {As2} exhibits the lowest As/Ca ratio (Fig. 4d).

Speciation of arsenic

The speciation maps of As(III) and As(V) revealed that the As(III) distribution exhibited a more diffuse pattern (Fig. 5a), while the As(V) distribution was predominantly defined by a globular pattern (Fig. 5b). The occurrence of organic material in the globular distribution was confirmed by CLSM analysis. The fluorescence emission of the globules with a maximum at 470 nm appeared similar to the one obtained in the organic area of the fresh microbialite (Fig. S4). This suggests that the main component forming the globules comprised organic material.

To better evaluate the difference between As(III) and As(V) distributions, several XANES points were collected in both the diffuse and globular regions (Fig. 5c). The XANES spectra collected in the diffuse regions showed a higher contribution of As(III) than As(V) (Fig. 5c, pt1), while the XANES spectra collected in the globules showed a higher contribution of As(V) than As(III) (Fig. 5c, pt2). This is also confirmed by the calculated As(V)/As(III) ratio (Fig. 4d), i.e. the As(V)/As(III) ratio decreases from the globular trend (labeled {As1} and marked in green) to the more diffuse trend (labeled {As3} and marked in light blue). No As(0) was identified in the XANES analysis.

DISCUSSION

The presence of organic-rich globules containing mainly arsenic ({As1}, Fig. 4) accumulated in specific zones of the microbial mats can be explained by different mechanisms. Investigations in modern sediments and bacterial cultures have addressed that prokaryotes are able to assimilate, methylate, detoxify and respire arsenic (Stolz *et al.*, 2006). Prokaryotes have developed strategies to detoxify arsenic, such as the *ars* gene (Páez-Espino *et al.*, 2009) and the methylation of As species (Bentley & Chasteen, 2002), but also to actively use arsenic compounds in their metabolism for obtaining energy or to support photosynthetic carbon fixation (Oremland *et al.*, 2005; van Lis *et al.*, 2013). In addition, arsenic compounds expelled from microbial activities can likely interact with the functional groups of the extrapolymeric matrix (EPS) (Braissant *et al.*, 2007). These functional groups deprotonate as a function of pH, and will lead to a higher overall negative charge for EPS in alkaline

conditions, such as those in Laguna Diamante. Positively charged ions, such as Ca^{2+} and Mg^{2+}, can form bidentate bonds with low-molecular-weight organic carbon (Braissant *et al.*, 2009), but also with negatively charged ions, such as arsenic oxyanions. In addition to this mechanism, active element cycling may also create globules of metal(loid) compounds in the organic matrix (whether this comprises EPS or microbial cells). The local environment plays then a crucial role for the metal(loid)s distribution, creating micro zones with oxidized or reduced elements. For instance, accumulation of As(III) or As(V) through detoxification reactions or bioenergetics reactions (see below), such as anoxygenic phototrophy, chemolithoautotrophic oxidation (e.g. of arsenate and sulphide) or arsenite oxidation may result in the incorporation of arsenic in the EPS.

Laguna Diamante microbialites grow in a hypersaline alkaline high-altitude lake with severe conditions, such as high UV radiation, low O_2 pressure and very low rainfall (table 1). In such an environment, the role of photosynthesis to convert inorganic carbon into organic biomass is usually the dominant metabolic pathway (Knoll & Bauld, 1989). In addition, the Diamante microbial metagenome suggests that methanogenesis is also an important metabolic process in this environment (Rascovan *et al.*, 2016). Methanogenic metabolism has also been observed in other high-altitude Andean lakes (Maldonado MJ *et al.*, 2018) and most likely also occurred in Precambrian lakes with similar conditions, such as the 2.7 billion-year-old anoxygenic Tumbiana lake (Eigenbrode & Freeman, 2006; Sforna *et al.*, 2014; Lepot *et al.*, 2019).

Methanogenic respiration produces methane, which can be incorporated as organic carbon into biomass through oxidation. Together with methane oxidation, nitrification (i.e. the oxidation of ammonia to nitrite and nitrate) is also likely taking place in Laguna Diamante microbialites, similar to what has been observed for related Andean lakes, such as Socompa and Titicaca Lake (Vincent *et al.*, 1985; Farías *et al.*, 2013). Methanotrophic and nitrification-denitrification reactions need strong oxidants, such as oxygen, ferric iron, sulphate or any other available electron acceptor. These oxidants are potentially delivered by photosynthetic reactions. However, the precise nature of these possible candidates has not yet been identified. Similar as in other high-altitude lakes, the water column of Laguna Diamante contains low saturation levels of oxygen due to its high altitude, resulting in limited oxygen availability to be used as electron acceptor for methanotrophic or nitrification-denitrification pathways (i.e. Vincent *et al.*, 1985, Visscher *et al.*, in prep).

Anoxygenic photosynthesis, using iron as an electron donor, cannot be significant since no iron-bearing minerals were detected in the microbialites of Laguna Diamante. On the other hand, anoxygenic phototrophs using reduced sulfur as electron donor, are common in hypersaline environments (Visscher *et al.*, 1992; Dupraz *et al.*, 2013; Pace *et al.*, 2018). Several anoxygenic phototrophs that use sulfur can also use other electron donors, such as As(III). For instance, phototrophic sulfide oxidizers of Diamante, such as *Chloroflexus aurantiacus*, have been reported to contain arsenite oxidation gene, A*io* (Rascovan *et al.*, 2016), which may produce As(V). Some anoxyphototrophs can use sulfide for their metabolic activities, but other electron donors, such as As(III). In this case, As(III) may be a potential electron donor for anoxygenic photosynthesis and denitrification in Laguna Diamante microbialites. The arsenite can be used instead of sulfide as electron donors by some purple sulfur bacteria that live in As-rich environments. This has been observed in *Ectothiorhodospira* sp. in a Hot Spring Photosynthetic Biofilm at Mono Lake (Hoeft *et al.*, 2010). As(V), in turn, is then available as an electron acceptor for chemolithoautotrophic or chemoorganoheterotrophic anaerobes capable of As(V) respiration, for which also a gene, *Arr*, has been detected in Laguna Diamante microbialites (Rascovan *et al.*, 2016). Thus, arsenic cycling is certainly feasible in Laguna Diamante microbialites. Evidence for arsenic cycle has been reported in other high-altitude lakes (Lara *et al.*, 2012; Farías *et al.*, 2013; Kurth *et al.*, 2017; Ordoñez *et al.*,

2018; Sancho-Tomás *et al.*, 2018) and in similar extant environments, such as Mono Lake and Searles Lakes (Oremland *et al.*, 2005; Kulp *et al.*, 2006, 2008; van Lis *et al.*, 2013; Edwardson & Hollibaugh, 2017; Saunders *et al.*, 2019). Remarkably, the sequences for arsenite oxidases and respiratory arsenate reductase from Laguna Diamante microbialites have been identified in haloarchaea (Rascovan *et al.*, 2016) and further research performed with Haloarcheae isolated from the same biofilm demonstrated the expression of this *AioA* gene under As growth (Ordoñez *et al.*, 2018). Divergence in the sequences of haloarchaea *AioA* and *ArrA* genes and the wide geographical distribution of the species that harbour them, could indicate a long evolutionary history of these enzymes in haloarchaea. It is thus likely that arsenic metabolisms may have been essential on the anoxic Precambrian Earth. This notion is supported by the evidence of a complete arsenic cycle taking place in 2.7 billion-year-old stromatolites from Tumbiana, Australia (Oremland *et al.*, 2009; Sforna *et al.*, 2014).

Detoxification reactions can also expel arsenic into the EPS. This mechanism cannot be excluded as genes related to detoxification mechanisms, particularly the *Ars* operon, were detected in the Diamante microbial metagenome (Rascovan *et al.*, 2016). The *Ars* operon promote a multistep process of methylation and redox reactions followed by formation of organoarsenic intermediates, like arsenosugars or arsenolipids (Bentley & Chasteen, 2002) to eliminate intracellular arsenic (Páez-Espino *et al.*, 2009) and it may also locally release several arsenic compounds. Although the involved reactions are still not well understood (Couture *et al.*, 2013; Huertas *et al.*, 2014), it has been suggested that methylation reactions may be used as an (supplementary) energy source (Yamamura & Amachi, 2014). Methylation and excretion of arsenic have been estimated to originate during the Archaean eon (Chen *et al.*, 2020). Together with the *Ars* operon, other detoxifying genes such as *ArsB* and *Acr3* arsenite efflux pumps have also been detected in the Diamante microbial metagenoma (Rascovan *et al.*, 2016). Hence, detoxification process is likely to occur in the studying microbialites. Detoxifying genes are present in most of the organisms that live in As-rich environments, from humans (Schlebusch *et al.*, 2013) to microbial living in shallow submarine hydrothermal ecosystems along the Hellenic Volcanic (Fru *et al.*, 2018). In any case, the products of both bioenergetics and detoxification reactions will eventually be expelled from the cell and accumulate in the EPS.

When the surface biofilm grows upward, the deeper layers of the microbialite undergo early and slow heterotrophic degradation and ultimately diagenetic alteration, leading to the fossilization of the microbialite (Dupraz & Visscher, 2005). It is in this process the imprint of specific metabolic activity can be preserved. A preliminary study of processes taking place in microbialites from Bahamas during diagenesis evaluated the metal(loid)s association and distribution within an extant stromatolite down to relic layers (~2 kyr) (Sforna *et al.* 2017). The ongoing changes in the elemental distribution patterns through early diagenesis were traced from the centimetre to the micrometer scale. Remarkably, the metal(loid)s distribution at the bottom of the mat was both homogeneous (due to passive absorption of elements within the mat) and heterogeneous. In particular, the As-bearing organic globules embedded in carbonate grains were not associated with any other metal. The As globules were attributed to As-metabolizing microorganisms, showing the potential of this element to be interpreted as a biosignature in modern system as well as in the rock record (Sforna *et al.*, 2017). Although difficult to constrain the processes involved (probably both, energetic and detoxification pathways), we propose below a potential mechanism of the transformation of the arsenic fingerprints, from the organic-rich, irregular arsenic globules in the newly formed surface layer to the early diagenetic stage (Fig. 6). This might be useful for identifying past biologically active in the ancient rock record.

During the first step, arsenic cycling occurs through microbe-mediated reactions (Fig. 6a), which releases different As compounds in the environment. During a second step, these As species bound to the organic matrix, whether interacting with the functional groups of the EPS or with microbial cells, and form irregular globules (Fig. 6b) such as those shown in Figure 4, {As1}. Once released into the extracellular matrix (EPS), the distribution of the arsenic species may vary depending on the mobility of the released arsenic species and the chemical conditions of the extracellular medium. As such, the As(III) distribution displayed a more diffuse pattern (Fig. 5a) compared to As(V), which shows a globular morphology (Fig. 5b). Arsenite is considered to be more mobile than arsenate (Smedley & Kinniburgh, 2002) because As(III) exists predominately as a neutral species at mildly basic conditions (PKa of H_3AsO_3= 9.32, 12.10, 13.41) (Sø et $al.$, 2008; Yokoyama et $al.$, 2012). Contrary, As(V), is a stronger acid (PKa = 2.24, 6.96, 11.50), being more readily immobilized in the microbial mat through interactions with the functional groups of EPS, such as carboxyl, phosphate, amino, or sulfur groups (Braissant et $al.$, 2007). During the third step of the proposed mechanism, precipitation of $CaCO_3$ takes place (Fig. 4, {As2}). The carbonate mineral replacing the EPS (Dupraz & Visscher, 2005) then incorporates As (Fig. 6c).

Microbial metabolism plays an important role in carbonate precipitation, mainly through inducing pH changes (Dupraz & Visscher, 2005). Processes, such as anoxygenic phototrophy and sulfate reduction (and by extension also arsenate reduction) contribute to $CaCO_3$ precipitation (Dupraz et $al.$, 2009). Laboratory studies of the incorporation of As in the calcite structure have shown that abiotic incorporation processes result in predominantly As(V) uptake (e.g. (Sø et $al.$, 2008; Yokoyama et $al.$, 2012)). This can be explained on the basis of the different chemical nature of arsenite and arsenate oxyanions (Sø et $al.$, 2008; Yokoyama et $al.$, 2012). The first one exists predominantly as a neutral species while the second one is a stronger acid, forming a negative oxyanion that favours not only the interactions with EPS but also the adsorption and incorporation of As(V) into the calcite structure (Yokoyama et $al.$, 2012; Renard et $al.$, 2015). The presence of As(III) in the calcite structure has been related with the occurrence of biological process, for example, a significant fraction of As(III) has been detected in natural calcite from travertine deposits of Central Italy (Di Benedetto et $al.$, 2006; Bardelli et $al.$, 2011). More recently, the incorporation of As(III) was detected in biogenic calcite precipitated from bacteria cultures but not in the abiotic control incubations (Catelani et $al.$, 2018). Hence, the presence of As(III) in the globules ({As1} in fig.4) and in the high-carbonate areas ({As2} in fig. 4) strongly indicates that the incorporation of As into the structure is microbial mediated (Fig.5e). Finally, the EPS is gradually replaced by micrite (Fig. 6d) (Dupraz & Visscher, 2005), which then can incorporate the remaining more diffuse and mobile As(III) excreted by the arsenic respiring bacteria. This is supported by the increase of As(III) in the Ca-rich globules/carbonate zone compared to the organic-rich globules (see As(V)/As(III) ratio of Fig. 4e).

CONCLUDING REMARKS

The co-occurring presence of two oxidation states, As(III) and As(V), discovered in this study represents the first geochemical evidence of microbial-mediated arsenic cycling in Laguna Diamante microbialites, supporting the metagenomic analysis published by Rascovan and co-workers (Rascovan et $al.$, 2016). We propose a mechanism for preserving the As-microbial mediated cycle in the carbonate structure of microbialites from initial lithification to early diagenesis. This might be extended to the fossil record, where further studies may lead to development of an arsenic fingerprint for detection of life in the fossil record from the early Earth and, possibly, from other planets such as Mars.

ACKNOWLEDMENTS

REFERENCES

Alexandratos VG, Elzinga EJ, Reeder RJ (2007) Arsenate uptake by calcite: Macroscopic and spectroscopic characterization of adsorption and incorporation mechanisms. *Geochimica et Cosmochimica Acta* **71**, 4172–4187.

Bardelli F, Benvenuti M, Costagliola P, Di Benedetto F, Lattanzi P, Meneghini C, Romanelli M, Valenzano L (2011) Arsenic uptake by natural calcite: An XAS study. *Geochimica et Cosmochimica Acta* **75**, 3011–3023.

Bentley R, Chasteen TG (2002) Microbial methylation of metalloids: arsenic, antimony, and bismuth. *Microbiology and molecular biology reviews: MMBR* **66**, 250–271.

Bergamaschi A, Medjoubi K, Messaoudi C, Marco S, Somogyi A (2016) MMX-I: data-processing software for multimodal X-ray imaging and tomography. *Journal of Synchrotron Radiation* **23**, 783–794.

Bischoff JL, Herbst DB, Rosenbauer RJ (1991) Gaylussite formation at mono lake, california. *Geochimica et Cosmochimica Acta* **55**, 1743–1747.

Braissant O, Decho AW, Dupraz C, Glunk C, Przekop KM, Visscher PT (2007) Exopolymeric substances of sulfate- reducing bacteria: interactions with calcium at alkaline pH and implication for formation of carbonate minerals. *Geobiology* **5**, 401–411.

Braissant O, Decho AW, Przekop KM, Gallagher KL, Glunk C, Dupraz C, Visscher PT (2009) Characteristics and turnover of exopolymeric substances in a hypersaline microbial mat. *FEMS Microbiology Ecology* **67**, 293–307.

Cabral AR, Beaudoin G (2007) Volcanic red-bed copper mineralisation related to submarine basalt alteration, Mont Alexandre, Quebec Appalachians, Canada. *Mineralium Deposita* **42**, 901–912.

Carignan J, Hild P, Mevelle G, Morel J, Yeghicheyan D (2001) Routine Analyses of Trace Elements in Geological Samples using Flow Injection and Low Pressure On- Line Liquid Chromatography Coupled to ICP MS: A Study of Geochemical Reference Materials BR, DR-N, UB- N, AN- G and GH. *Geostandards Newsletter* **25**, 187–198.

Catelani T, Perito B, Bellucci F, Lee SS, Fenter P, Newville M, Rimondi V, Pratesi G, Costagliola P (2018) Arsenic uptake in bacterial calcite. *Geochimica et Cosmochimica Acta* **222**, 642–654.

Chen S-C, Sun G-X, Yan Y, Konstantinidis KT, Zhang S-Y, Deng Y, Li X-M, Cui H-L, Musat F, Popp D, Rosen BP, Zhu Y-G (2020) The Great Oxidation Event expanded the genetic repertoire of arsenic metabolism and cycling. *Proceedings of the National Academy of Sciences* 202001063.

Chi Fru E, Somogyi A, Albani AE, Medjoubi K, Aubineau J, Robbins LJ, Lalonde SV, Konhauser KO (2019) The rise of oxygen-driven arsenic cycling at ca. 2.48 Ga. *Geology* **47**, 243–246.

Couture R-M, Rose J, Kumar N, Mitchell K, Wallschläger D, Van Cappellen P (2013) Sorption of Arsenite, Arsenate, and Thioarsenates to Iron Oxides and Iron Sulfides: A Kinetic and Spectroscopic Investigation. *Environmental Science & Technology* **47**, 5652–5659.

Di Benedetto F, Costagliola P, Benvenuti M, Lattanzi P, Romanelli M, Tanelli G (2006) Arsenic incorporation in natural calcite lattice: Evidence from electron spin echo spectroscopy. *Earth and Planetary Science Letters* **246**, 458–465.

Dupraz C, Fowler A, Tobias C, Visscher PT (2013) Stromatolitic knobs in Storr's Lake (San Salvador, Bahamas): a model system for formation and alteration of laminae. *Geobiology* **11**, 527–548.

Dupraz C, Reid RP, Braissant O, Decho AW, Norman RS, Visscher PT (2009) Processes of carbonate precipitation in modern microbial mats. *Earth-Science Reviews*, Microbial Mats in Earth's Fossil Record of Life: Geobiology **96**, 141–162.

Dupraz C, Visscher PT (2005) Microbial lithification in marine stromatolites and hypersaline mats. *Trends in Microbiology* **13**, 429–438.

Edwardson CF, Hollibaugh JT (2017) Metatranscriptomic analysis of prokaryotic communities active in sulfur and arsenic cycling in Mono Lake, California, USA. *The ISME Journal* **11**, 2195–2208.

Eigenbrode JL, Freeman KH (2006) Late Archean rise of aerobic microbial ecosystems. *Proceedings of the National Academy of Sciences of the United States of America* **103**, 15759–15764.

Etschmann BE, Donner E, Brugger J, Howard DL, Jonge MD de, Paterson D, Naidu R, Scheckel KG, Ryan CG, Lombi E (2014) Speciation mapping of environmental samples using XANES imaging. *Environmental Chemistry* **11**, 341–350.

Farías ME, Rascovan N, Toneatti DM, Albarracín VH, Flores MR, Poiré DG, Collavino MM, Aguilar OM, Vazquez MP, Polerecky L (2013) The Discovery of Stromatolites Developing at 3570 m above Sea Level in a High-Altitude Volcanic Lake Socompa, Argentinean Andes. *PLOS ONE* **8**, 1–15.

Fru EC, Callac N, Posth NR, Argyraki A, Ling Y-C, Ivarsson M, Broman C, Kilias SP (2018) Arsenic and high affinity phosphate uptake gene distribution in shallow submarine hydrothermal sediments. *Biogeochemistry* **141**, 41–62.

Gérard E, Ménez B, Couradeau E, Moreira D, Benzerara K, Tavera R, López-García P (2013) Specific carbonate–microbe interactions in the modern microbialites of Lake Alchichica (Mexico). *The ISME Journal* **7**, 1997–2009.

Hoeft SE, Kulp TR, Han S, Lanoil B, Oremland RS (2010) Coupled Arsenotrophy in a Hot Spring Photosynthetic Biofilm at Mono Lake, California. *Applied and Environmental Microbiology* **76**, 4633.

Huerta-Diaz MA, Delgadillo-Hinojosa F, Siqueiros-Valencia A, Valdivieso-Ojeda J, Reimer JJ, Segovia-Zavala JA (2012) Millimeter-scale resolution of trace metal distributions in microbial mats from a hypersaline environment in Baja California, Mexico. *Geobiology* **10**, 531–547.

Huertas MJ, López-Maury L, Giner-Lamia J, Sánchez-Riego AM, Florencio FJ (2014) Metals in Cyanobacteria: Analysis of the Copper, Nickel, Cobalt and Arsenic Homeostasis Mechanisms. *Life* **4**, 865–886.

Jones BF, Eugster HP, Rettig SL (1977) Hydrochemistry of the Lake Magadi basin, Kenya. *Geochimica et Cosmochimica Acta* **41**, 53–72.

Knoll AH, Bauld J (1989) The evolution of ecological tolerance in prokaryotes. *Earth and Environmental Science Transactions of the Royal Society of Edinburgh* **80**, 209–223.

Kulp TR, Hoeft SE, Asao M, Madigan MT, Hollibaugh JT, Fisher JC, Stolz JF, Culbertson CW, Miller LG, Oremland RS (2008) Arsenic(III) Fuels Anoxygenic Photosynthesis in Hot Spring Biofilms from Mono Lake, California. *Science* **321**, 967.

Kulp TR, Hoeft SE, Miller LG, Saltikov C, Murphy JN, Han S, Lanoil B, Oremland RS (2006) Dissimilatory arsenate and sulfate reduction in sediments of two hypersaline, arsenic-rich soda lakes: Mono and Searles Lakes, California. *Applied and Environmental Microbiology* **72**, 6514–6526.

Kurth D, Amadio A, Ordoñez OF, Albarracín VH, Gärtner W, Farías ME (2017) Arsenic metabolism in high altitude modern stromatolites revealed by metagenomic analysis. *Scientific Reports* **7**, 1024.

Lara J, Escudero-González L, Ferrero M, Chong-Díaz G, Pedrós-Alió C, Demergasso C (2012) Enrichment of arsenic transforming and resistant heterotrophic bacteria from sediments of two salt lakes in Northern Chile. *Extremophiles: Life Under Extreme Conditions* **16**, 523–538.

Lepot K, Williford KH, Philippot P, Thomazo C, Ushikubo T, Kitajima K, Mostefaoui S, Valley JW (2019) Extreme 13C-depletions and organic sulfur content argue for S-fueled anaerobic methane oxidation in 2.72 Ga old stromatolites. *Geochimica et Cosmochimica Acta* **244**, 522–547.

Li H, Xin HL, Muller DA, Estroff LA (2009) Visualizing the 3D Internal Structure of Calcite Single Crystals Grown in Agarose Hydrogels. *Science* **326**, 1244.

Lis R van, Nitschke W, Duval S, Schoepp-Cothenet B (2013) Arsenics as bioenergetic substrates. *Biochimica Et Biophysica Acta* **1827**, 176–188.

M. Soler M, Caffe P, Coira B, T. Onoe A, Kay S (2007) Geology of the Vilama caldera: A new interpretation of a large-scale explosive event in the Central Andean Plateau during the Upper Miocene. *Journal of Volcanology and Geothermal Research - J VOLCANOL GEOTHERM RES* **164**, 27–53.

Maldonado MJ, Albarracín VH, Lara JA, Ferrero MA, Farías ME (2018) Culture-dependent and -independent methods reveal dominance of halophilic Euryarchaeota in high-altitude Andean lakes. *Aquatic Microbial Ecology* **81**, 171–188.

Munoz EC, Mehic S, Saltikov C (2018) Arsenic Biogeochemical Cycling Under Extreme, Archean-like Conditions. *AGU Fall Meeting Abstracts* **43**.

Ordoñez OF, Rasuk MC, Soria MN, Contreras M, Farías ME (2018) Haloarchaea from the Andean Puna: Biological Role in the Energy Metabolism of Arsenic. *Microbial Ecology* **76**, 695–705.

Oremland RS, Kulp TR, Blum JS, Hoeft SE, Baesman S, Miller LG, Stolz JF (2005) A microbial arsenic cycle in a salt-saturated, extreme environment. *Science (New York, N.Y.)* **308**, 1305–1308.

Oremland RS, Saltikov CW, Wolfe-Simon F, Stolz JF (2009) Arsenic in the Evolution of Earth and Extraterrestrial Ecosystems. *Geomicrobiology Journal* **26**, 522–536.

Pace A, Bourillot R, Bouton A, Vennin E, Braissant O, Dupraz C, Duteil T, Bundeleva I, Patrier P, Galaup S, Yokoyama Y, Franceschi M, Virgone A, Visscher PT (2018) Formation of stromatolite lamina at the interface of oxygenic–anoxygenic photosynthesis. *Geobiology* **00**, 1–21.

Páez-Espino D, Tamames J, Lorenzo V de, Cánovas D (2009) Microbial responses to environmental arsenic. *Biometals: An International Journal on the Role of Metal Ions in Biology, Biochemistry, and Medicine* **22**, 117–130.

Rae Cho K, Kim Y-Y, Yang P, Cai W, Pan H, Kulak AN, Lau JL, Kulshreshtha P, Armes SP, Meldrum FC, De Yoreo JJ (2016) Direct observation of mineral–organic composite formation reveals occlusion mechanism. *Nature Communications* **7**, 10187.

Rascovan N, Maldonado J, Vazquez MP, Eugenia Farías M (2016) Metagenomic study of red biofilms from Diamante Lake reveals ancient arsenic bioenergetics in haloarchaea. *The ISME journal* **10**, 299–309.

Renard F, Putnis CV, Montes-Hernandez G, Ruiz-Agudo E, Hovelmann J, Sarret G (2015) Interactions of arsenic with calcite surfaces revealed by in situ nanoscale imaging. *Geochimica et Cosmochimica Acta* **159**, 61–79.

Ruggieri F, Saavedra J, Fernandez-Turiel JL, Gimeno D, Garcia-Valles M (2010) Environmental geochemistry of ancient volcanic ashes. *Journal of Hazardous materials* **183**, 353–365.

Sancho-Tomás M, Somogyi A, Medjoubi K, Bergamaschi A, Visscher PT, Driessche AES van, Gérard E, Farias ME, Contreras M, Philippot P (2018) Distribution, redox state and (bio)geochemical implications of arsenic in present day microbialites of Laguna Brava, Salar de Atacama. *Chemical Geology*.

Saunders JK, Fuchsman CA, McKay C, Rocap G (2019) Complete arsenic-based respiratory cycle in the marine microbial communities of pelagic oxygen-deficient zones. *Proceedings of the National Academy of Sciences* **116**, 9925.

Schlebusch CM, Lewis CM Jr, Vahter M, Engström K, Tito RY, Obregón-Tito AJ, Huerta D, Polo SI, Medina ÁC, Brutsaert TD, Concha G, Jakobsson M, Broberg K (2013) Possible positive selection for an arsenic-protective haplotype in humans. *Environmental health perspectives* **121**, 53–58.

Sforna MC, Daye M, Philippot P, Somogyi A, Zuilen MA van, Medjoubi K, Gérard E, Jamme F, Dupraz C, Braissant O, Glunk C, Visscher PT (2017) Patterns of metal distribution in hypersaline microbialites during early diagenesis: Implications for the fossil record. *Geobiology* **15**, 259–279.

Sforna MC, Philippot P, Somogyi A, Zuilen MA van, Medjoubi K, Schoepp-Cothenet B, Nitschke W, Visscher PT (2014) Evidence for arsenic metabolism and cycling by microorganisms 2.7 billion years ago. *Nature Geoscience* **7**, 811–815.

Smedley PL, Kinniburgh DG (2002) Chapter 1 Source And Behaviour Of Arsenic In Natural Waters. British Geological Survey, Wallingford, Oxon OX10 8BB, U.K.

Sø HU, Postma D, Jakobsen R, Larsen F (2008) Sorption and desorption of arsenate and arsenite on calcite. *Geochimica et Cosmochimica Acta* **72**, 5871–5884.

Solé VA, Papillon E, Cotte M, Walter P, Susini J (2007) A multiplatform code for the analysis of energy-dispersive X-ray fluorescence spectra. *Spectrochimica Acta Part B: Atomic Spectroscopy* **62**, 63–68.

Somogyi A, Medjoubi K, Baranton G, Le Roux V, Ribbens M, Polack F, Philippot P, Samama JP (2015) Optical design and multi-length-scale scanning spectro-microscopy possibilities at the Nanoscopium beamline of Synchrotron Soleil. *Journal of Synchrotron Radiation* **22**, 1118–1129.

Stolz JF, Basu P, Santini JM, Oremland RS (2006) Arsenic and selenium in microbial metabolism. *Annu Rev Microbiol* **60**, 107–130.

Sun H, Lloyd JR (2010) *Biological Chemistry of Arsenic, Antimony and Bismuth. Chapter VI.* John Wiley & Sons.

Vincent WF, Vincent CL, Downes MT, Richerson PJ (1985) Nitrate cycling in Lake Titicaca (Peru-Bolivia): the effects of high-altitude and tropicality. *Freshwater Biology* **15**, 31–42.

Visscher PT (2014) The role of arsenic cycling in carbonate precipitation in microbialites through time. In: *GSA Annual Meeting in Vancouver, British Columbia*.

Visscher PT, Ende FP van den, Schaub BEM, Gemerden H van (1992) Competition between anoxygenic phototrophic bacteria and colorless sulfur bacteria in a microbial mat. *FEMS Microbiology Letters* **101**, 51–58.

Witt-Eickschen G, Palme H, O'Neill HSC, Allen CM (2009) The geochemistry of the volatile trace elements As, Cd, Ga, In and Sn in the Earth's mantle: New evidence from in situ analyses of mantle xenoliths. *Geochimica et Cosmochimica Acta* **73**, 1755–1778.

Yamamura S, Amachi S (2014) Microbiology of inorganic arsenic: From metabolism to bioremediation. *Journal of Bioscience and Bioengineering* **118**, 1–9.

Yokoyama Y, Tanaka K, Takahashi Y (2012) Differences in the immobilization of arsenite and arsenate by calcite. *Geochimica et Cosmochimica Acta* **91**, 202–219.

FIGURE and TABLE CAPTIONS

Figure 1. Site location and view of the studied microbialite from Diamante Lake (Argentina). (a) Aerial view of Diamante Lake showing the *Galán* peak. The sampling site is marked by a red arrow. (b) Closer view of the sampling site. (c) Overview of the tubular build-up microbialites (corresponds with the black box shown in image b). Inset: Photograph of the living microbialite analyzed in this study, the arrow indicates the grow direction. (d) Zoom in of the area outlined in (c) showing the cross section of the Diamante microbialites. The analyzed area of Fig. 3a is marked by a black box.

Figure2. SEM images (*left*) and EDX analysis (*right*) of the area investigated using synchrotron techniques. Calcite precipitates, showing the As-Ca intercorrelation {As2} in the carbonate layer (a) and in the globules (b). Image (b) corresponds with the white rectangle in Fig. 2b. The arrows indicate the location where the X-ray beam was focused.

Figure 3. Large field of view multi-technique maps of the sample area marked by the red box in the 100 µm-thick polished section (a), showing the transmission image (b) and the distribution of As, Ca and Fe (c, d and e). The yellow square in (c) indicates the area where the high resolution map was performed. The color scale indicates the square root of the XRF intensities where blue represents the background intensity (i.e. below detection limit) and red represents the maximum measured intensity (see main text for details).

Figure 4. (a) RGB image of the distribution of As(green), Ca(red) and Fe(blue) in the area indicated in Fig. 3c. Blue arrows indicate the Fe regions. (b) Image of the four main clusters of PCA score results characteristics for the elemental variation of As, Ca and Fe. Dark blue represents the background. As

versus Ca (*left*) and As versus Fe (*right*) intercorrelation diagrams: {As1, green} corresponds to the globular distribution of As and it is partially correlated with Ca; {As2,red} corresponds with the carbonate areas and reflects the spatial overlap between As and Ca; {As3, light blue} corresponds with the diffused distribution of As and it is partially correlated with Fe and Ca; and {As4, orange} corresponds with the areas where Ca is mostly alone with no or only minor contributions of As or Fe. (d) As(V)/As(III) and As/Ca ratios of the pixel counts in the specific areas inferred by PCA and clustering analysis, showed in panel b: {As1} in green, {As2} in dark red, and {As3} in light blue.

Figure 5. XANES maps of (a) an As(III) dominanted region and (b) an As(V) dominanted region, with an inset view of the globular sample region marked by the white rectangle for (d) As(III) contribution and (e) As(V) contribution. Dark blue indicates the background. (c) XANES spectra at the As k-edge obtained in two representative areas where either As(III) (pt1, As-diffused area, {As3}) or As(V) (pt2, As-globular area, {As1}) is most abundant. The three black curves correspond to As_2O_3 and As_2O_5 standards.

Figure 6. A tentative model of the transformation of arsenic fingerprints from an organic-rich active metabolic area up to the early diagenesis stage. (a) Arsenic cycling is promoted due to microbial activities. (b) Arsenic species interact with the organic matrix accumulating in zones with a higher concentration of organic material. The dotted circle marks the As-EPS globular distribution with higher contribution of As(V) (e.g. {As1}, Fig. 4), while a more diffuse trend with higher contribution of As(III) (e.g. {As3}, Fig. 4) is located around the dotted circle. The organic material (EPS) is shown as white background. (c) Precipitation of $CaCO_3$ takes place in the globular distribution and arsenic is retained in calcite precipitates (e.g. {As2}, Fig. 4). (d) Finally, EPS is gradually replaced by micrite (e.g. top right corner of Fig. 4b, {As2}).

Table 1. Physicochemical properties of the water column at the sample locality. Measurements shown indicate the minimum and maximum values observed during a 24-hr period. The lowest values for pH, temperature of the air and water and light intensity were measured just before sunrise, around 6am in the morning. The maximum values reflect observations made early- to mid-afternoon during peak photosynthetic activity.

Table 2. Bulk major and trace element concentrations of Laguna Diamante microbialites.
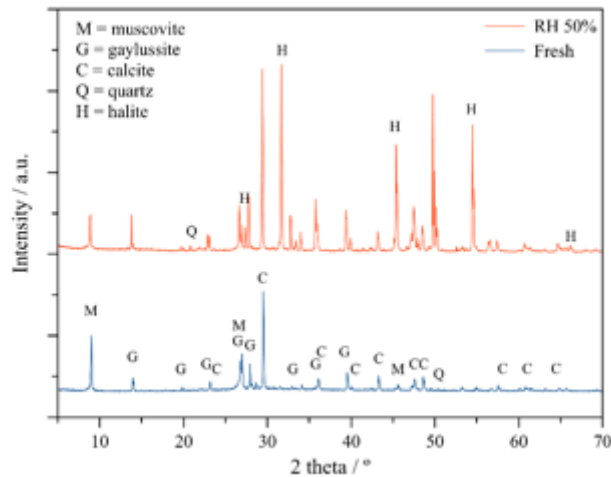
Supp. info

Figure SI1. Power X-ray diffraction patterns obtained from Lake Diamante microbialites, showing predominantly calcite with minor quantities of gaylussite, muscovite and quartz (fresh sample, in blue). Halite precipitates when the relative humidity is decreases in the sample chamber (RH 50%, in red) confirming that this mineral is not formed inside of living microbialites
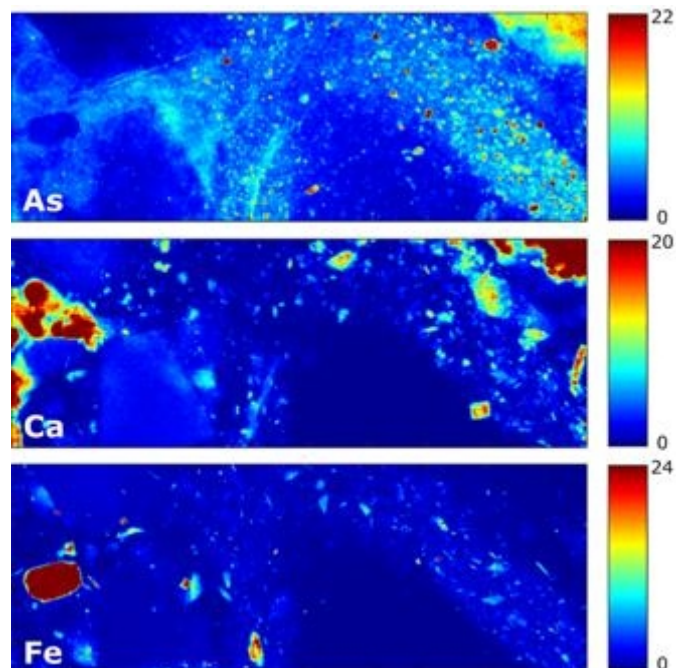

Figure SI2. XRF maps of the boxed area in Fig. 3c showing the distribution patterns of As, Ca and Fe. The colored scale indicates the square root of the XRF intensities: the background intensity (in blue, below detection limit) and the maximum measured intensity (in red). Dimensions of the map is 450 μm x 175 μm. Mapping was performed using a 0.5 μm x 0.5 μm incremental step.
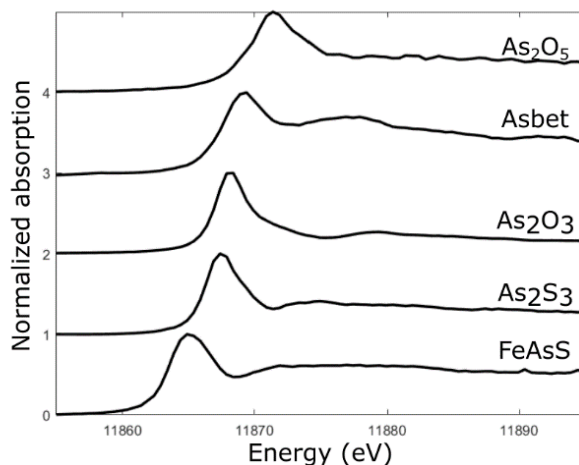
Figure SI3. XANES spectra of the measured standards. The X-ray energy points defined for XANES mapping correspond to the energy at the maximum intensity of: FeAsS, As_2S_3, As_2O_3, Asbet and As_2O_5 and to a medium energy point between Asbet and As_2O_5. Two additional energy points were selected, corresponding to the pre- and far away As K-edge.
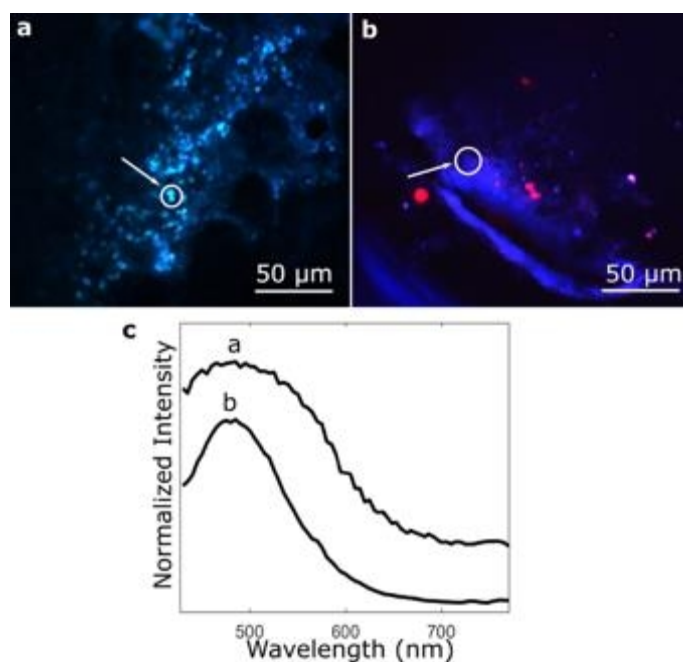
Figure S4. (a) Fluorescence map emitted in the range 435 – 796 nm following an excitation at 405 nm in the boxed area shown in Figure 2a and (b) in a fresh section of the studied microbialite. (c) Fluorescence emission spectra obtained with an excitation at 405 nm on the globular area (spectrum a, showing an example with the white circle on panel a) and the EPS in the fresh section, represented by blue color (white circle on panel b). The red color emitted in panel b corresponds to features containing chlorophyll and the black color corresponds to the background (spectra not shown).

Table 1. Physicochemical properties of the water column at the sample locality. Measurements shown indicate the minimum and maximum values observed during a 24-hr period. The lowest values for pH, temperature of the air and water and light intensity were measured just before sunrise, around 6am in the morning. The maximum values reflect observations made early- to mid-afternoon during peak photosynthetic activity.

Physicochemical prop.	Laguna Diamante
pH	9.1-10.7
Temperature air (°C)	-8.1 – 19.4
Temperature water (°C)	1.8 – 21.2
Conductivity (mS/cm)	204 ± 15
Salinity (g/L)	170 - 184
sLight intensity ($\mu E/m^2 \cdot s$)	0- 2188 ± 113
UV-AB (W/m^2)	71.3 ± 8.8
Arsenic (μM)	2272 ± 881
Sulfide (μM)	< 2
Sulfate (mM)	106.4 ± 4.5
Nitrate (μM)	1.37 ± 0.34
Chloride (mM)	2595 ± 43
Carbonate (mM)	144 ± 23
Ammonium (μM)	128 ± 54
Magnesium (mM)	0.82 ±0.11
Calcium (μM)	45.7 ± 3.9
Potassium (mM)	225.6 ± 18.0
Sodium (mM)	2189 ± 349

Table 2. Bulk major and trace element concentrations of Lake Diamante microbialites.

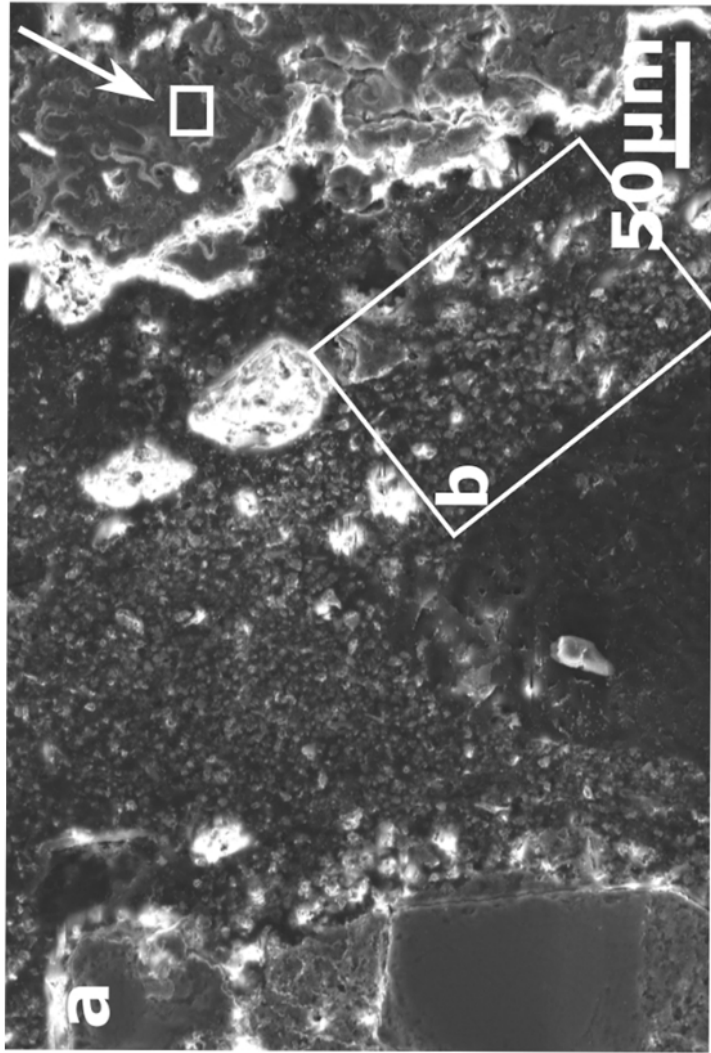| Sample	Concentration
Major oxide (%)	
CaO	30.3
SiO_2	11.8
Na_2O	10.1
MgO	1.1
Al_2O_3	1.0
K_2O	0.7
Fe_2O_3	0.3
LOI	44.2
Trace element (ppm)	
As	1372
Sr	1010
Cs	284
Rb	81
Ba	75
V, Sb, Zr	<20
Ge, Zn, Cr	<10

* LOI=Loss-on-ignition. It represents the fraction associated to water and organic matter.

Declaration of interests

☒   The authors declare that they have no known competing financial interests or personal relationships that could have appeared to influence the work reported in this paper.

☐The authors declare the following financial interests/personal relationships which may be considered as potential competing interests:
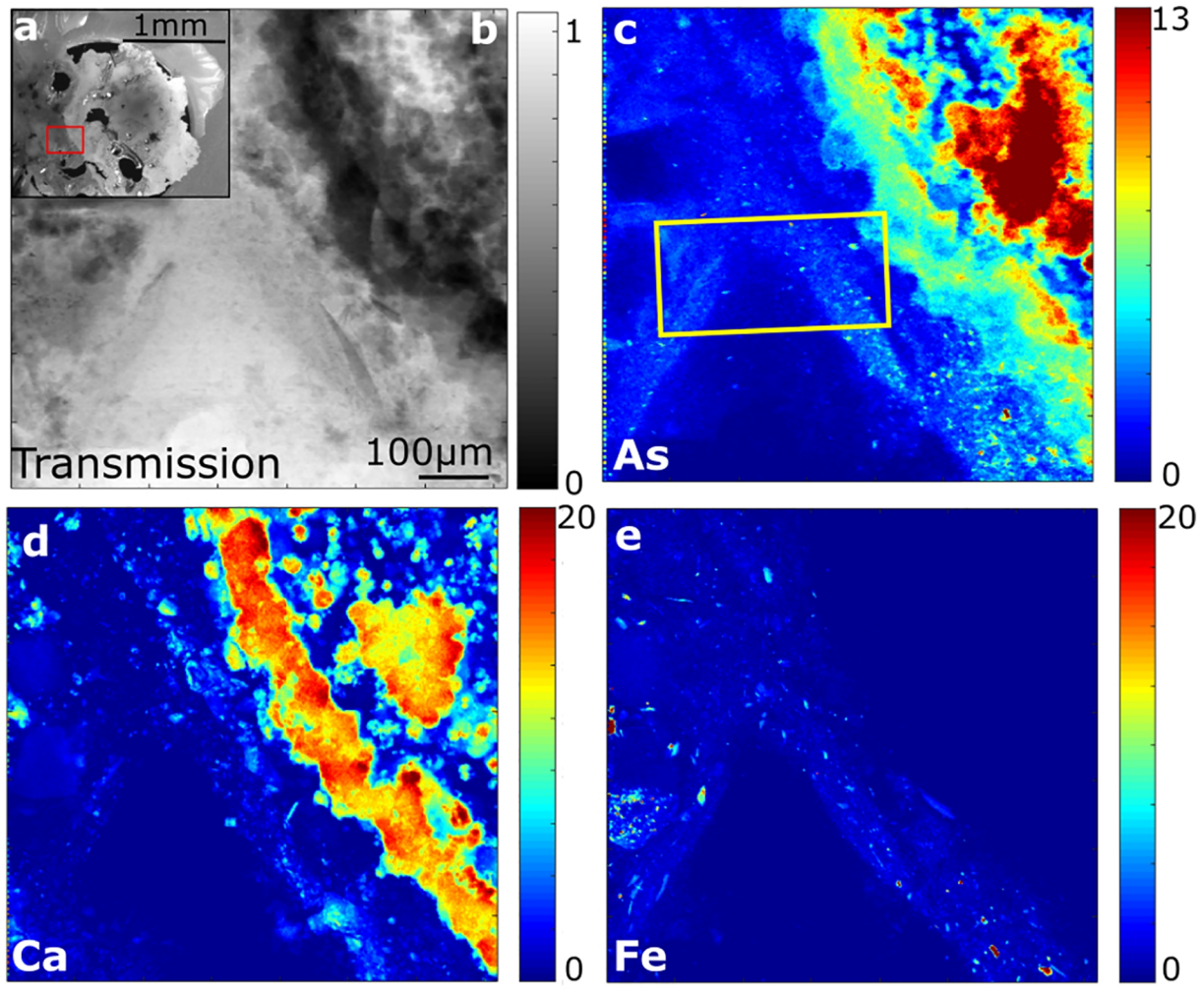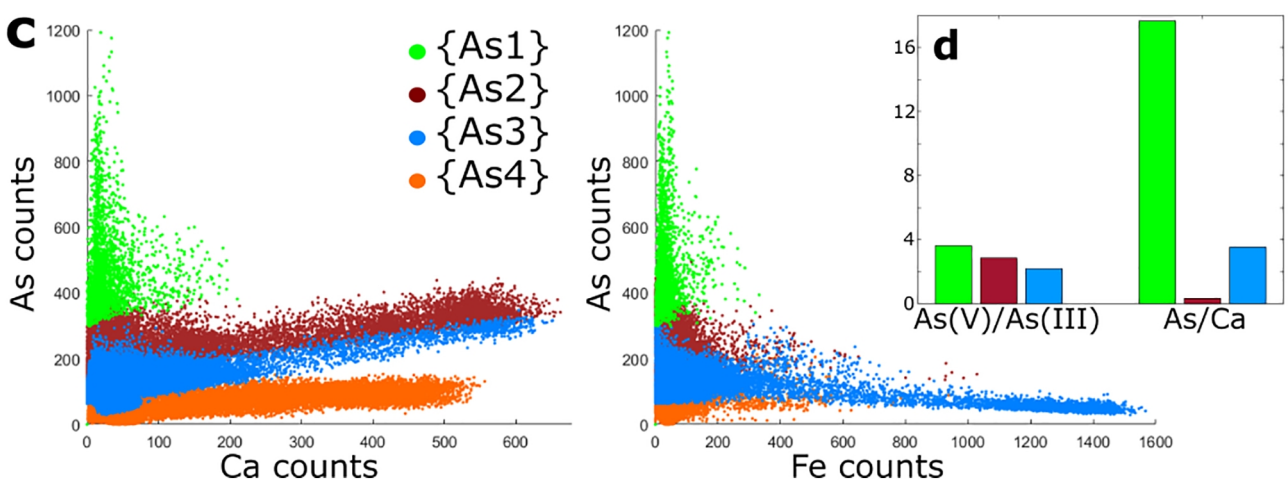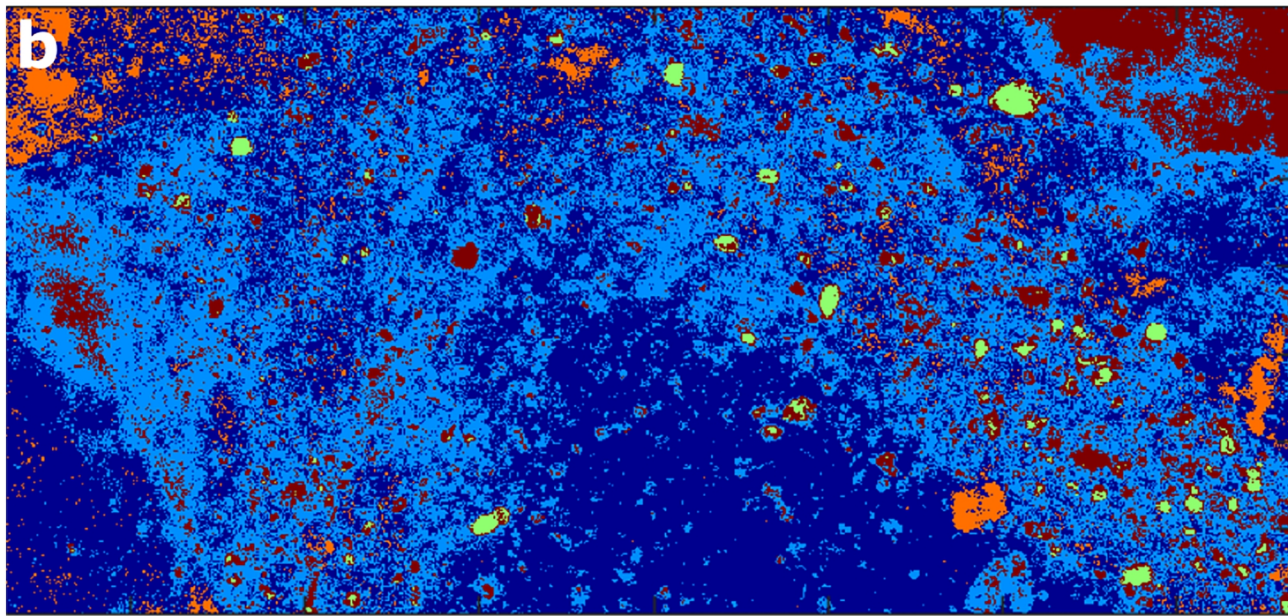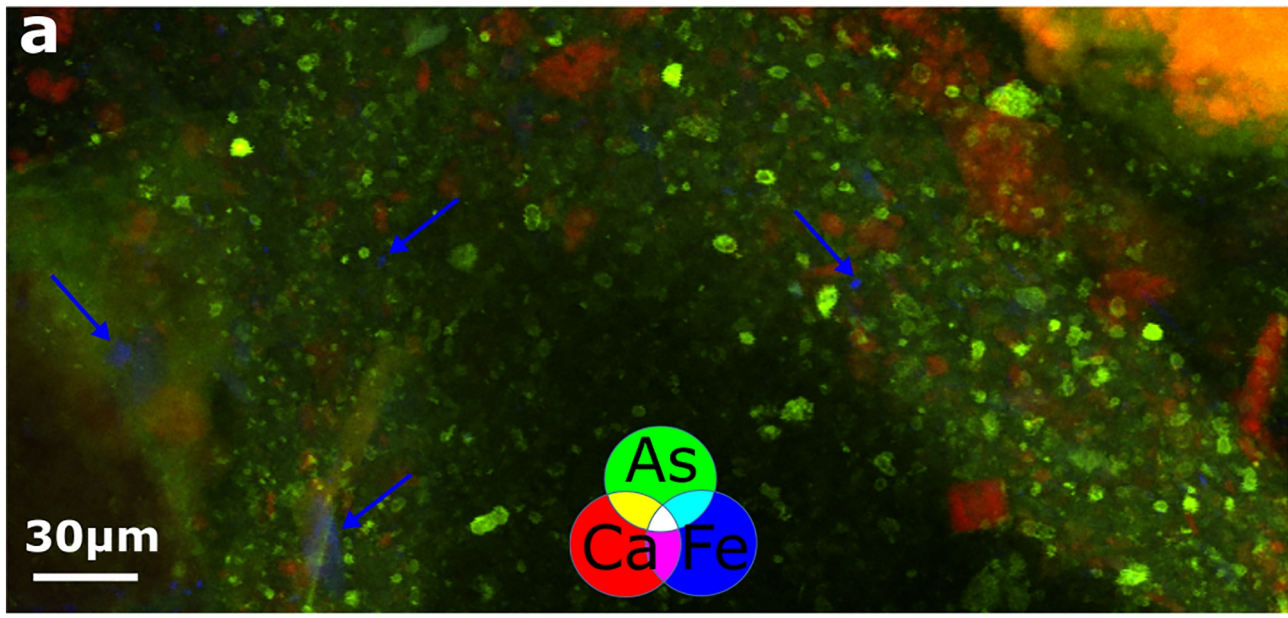
Figure 1

b

d

Galán peak

10 km

c

1cm

Figure 2

a

1mm

Transmission   100µm   b   1

c   13

As   0

d   20

Ca   0

e   20

Fe   0

Figure 3

Figure 4

a) As(III) contribution
pt1
pt2
30μm

b) As(V) contribution
pt1
pt2

d

e
5μm

c
Normalized absorption
pt2
pt1
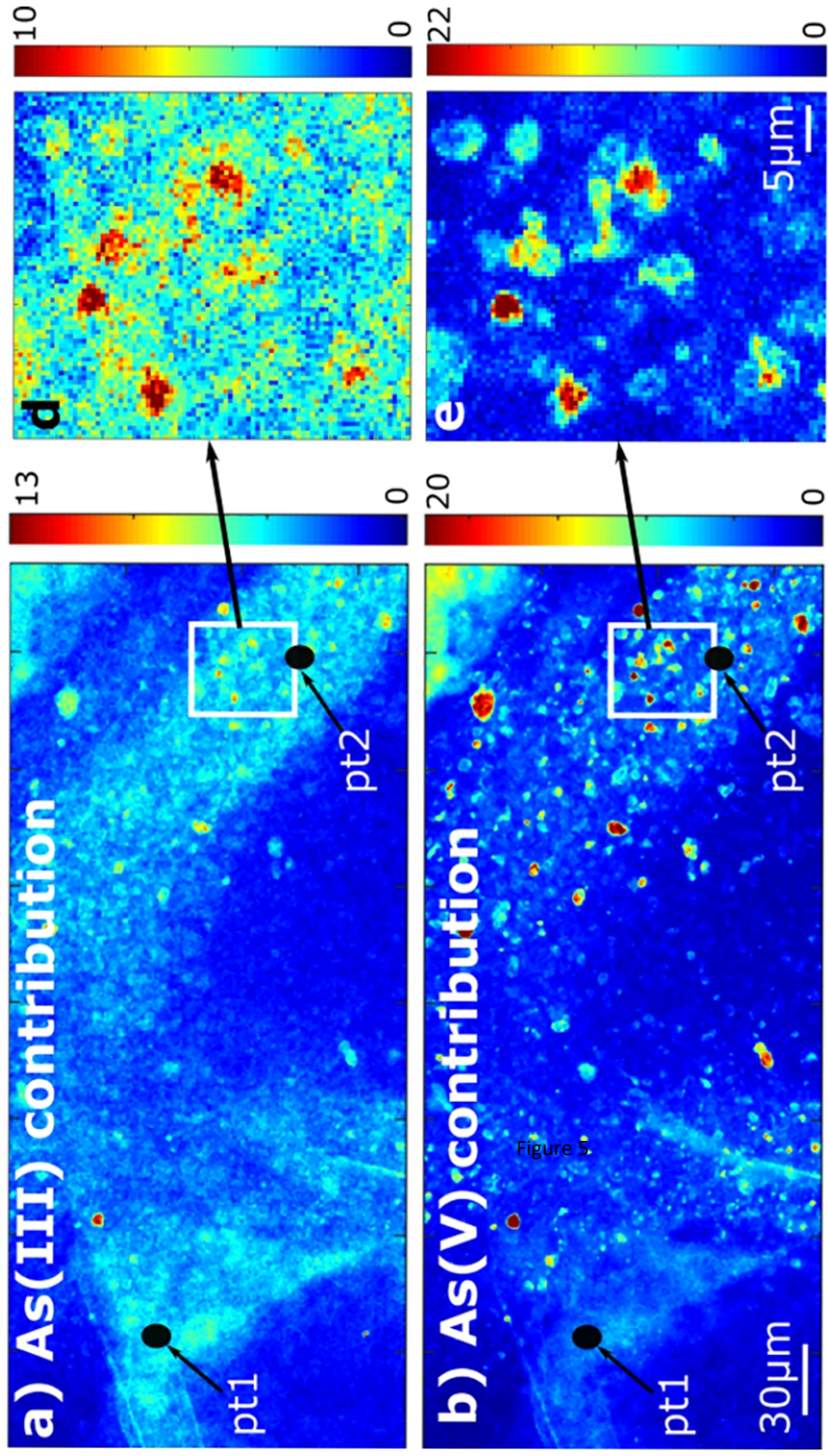As₂O₅
As₂O₃
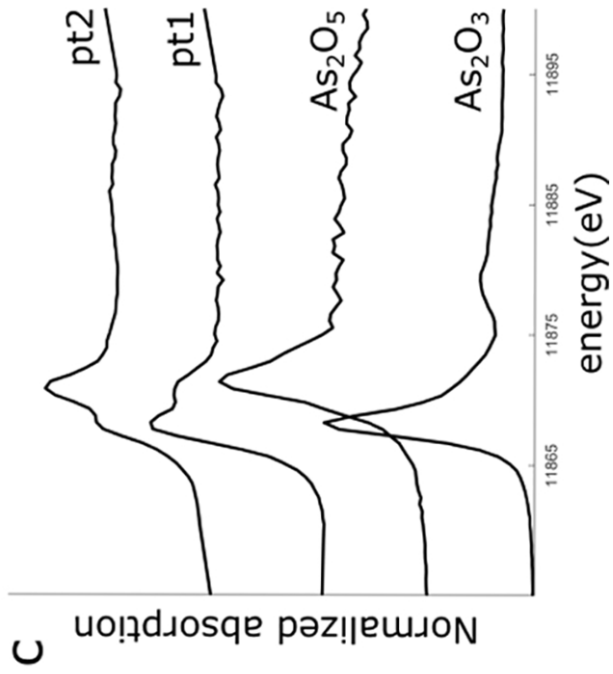energy(eV)
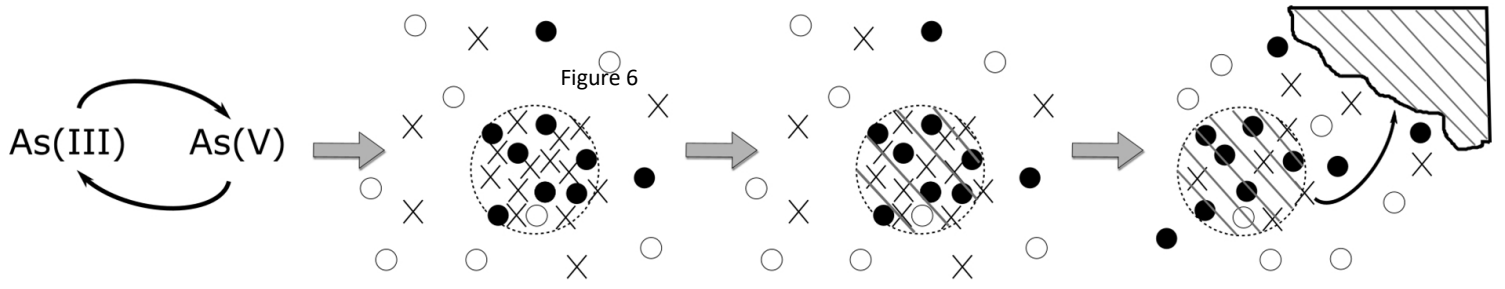11865 11875 11885 11895
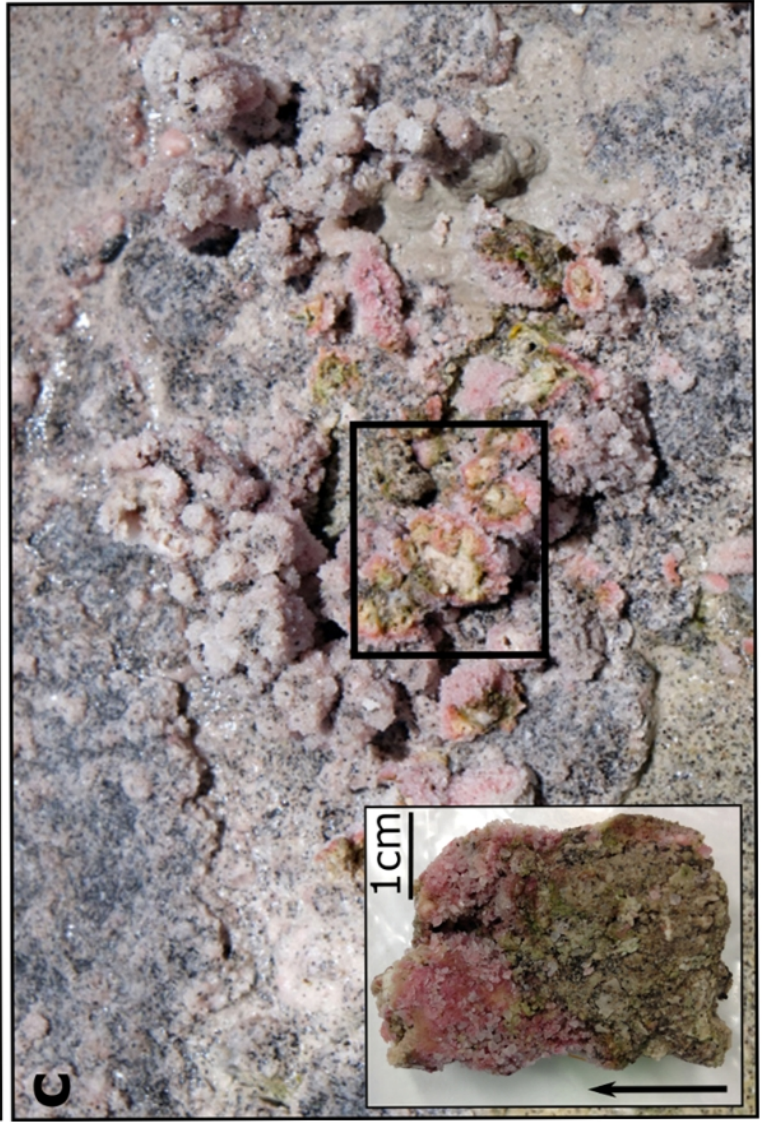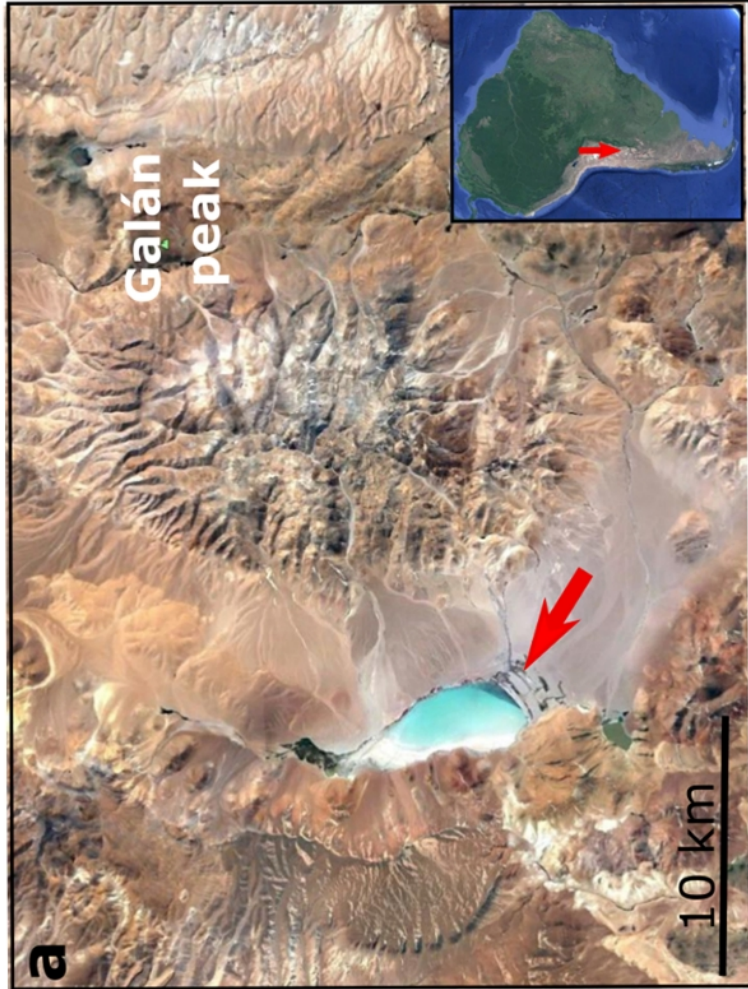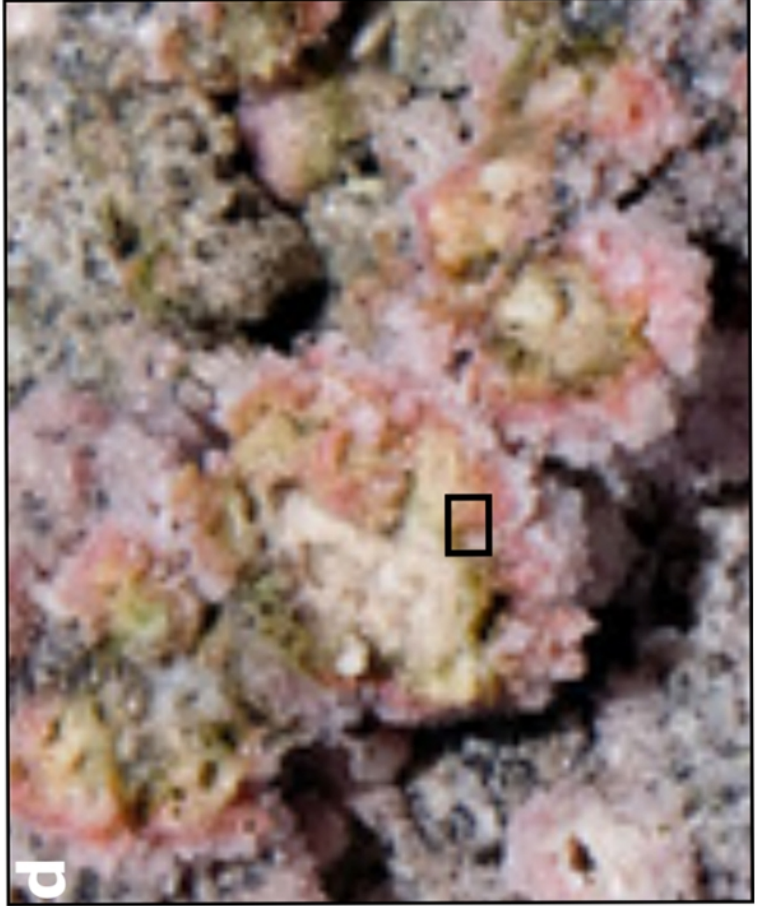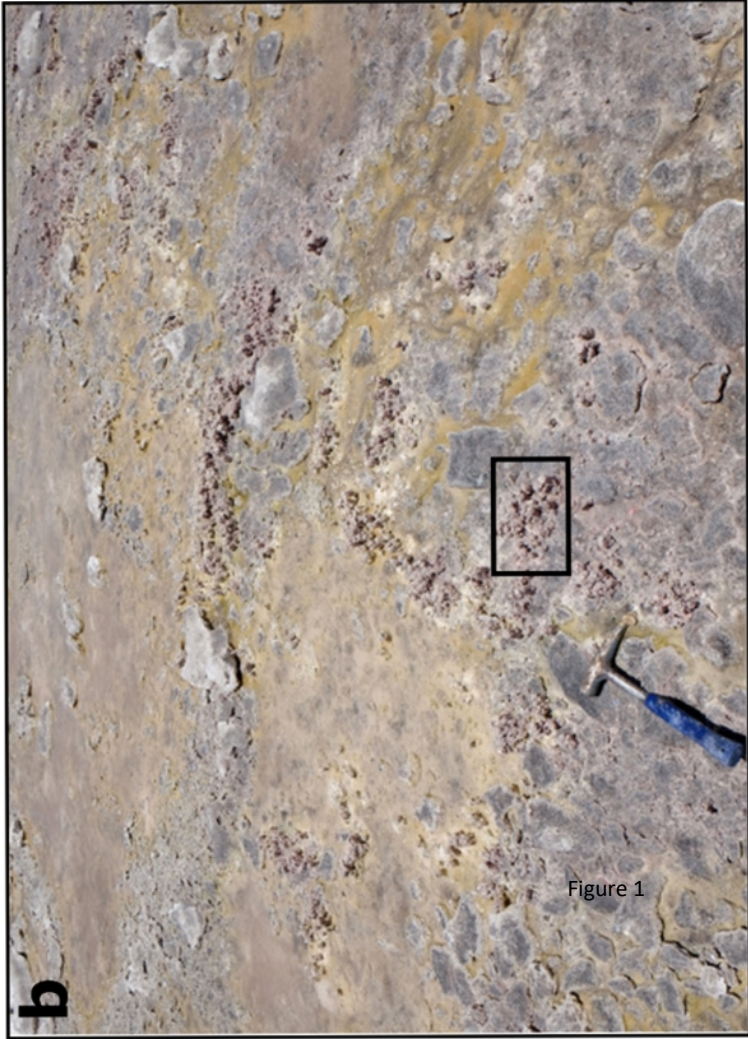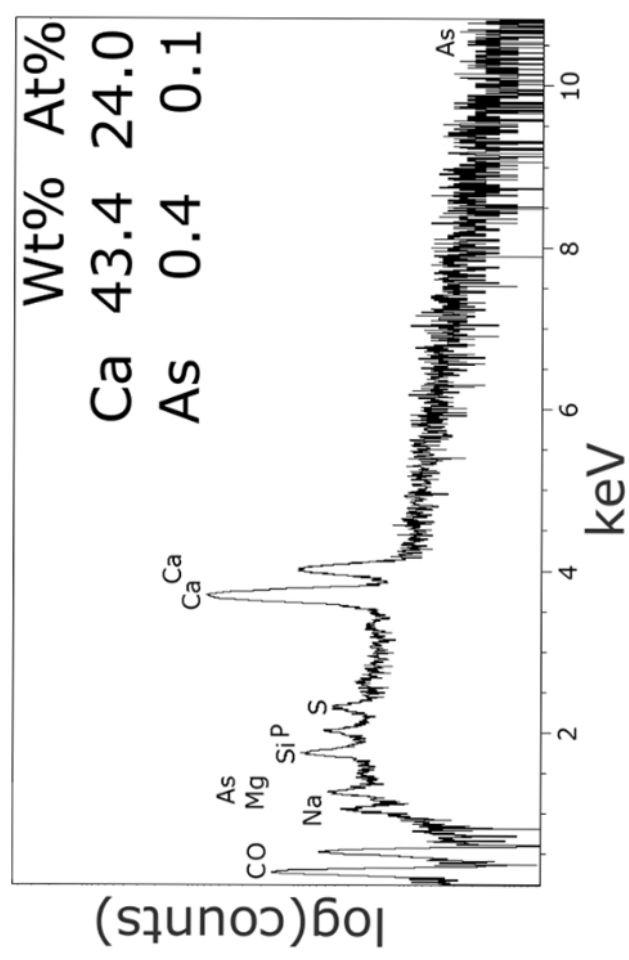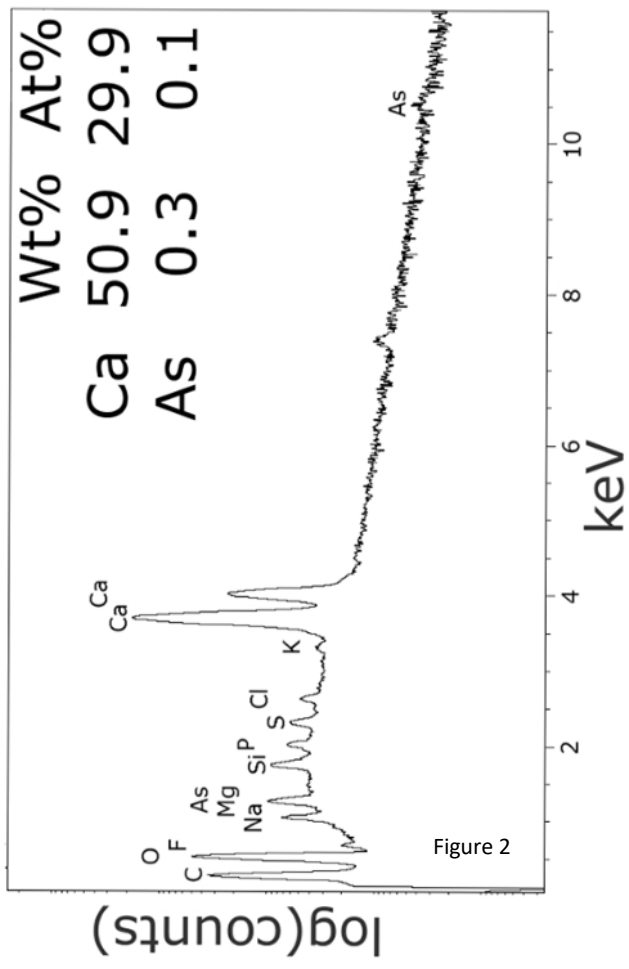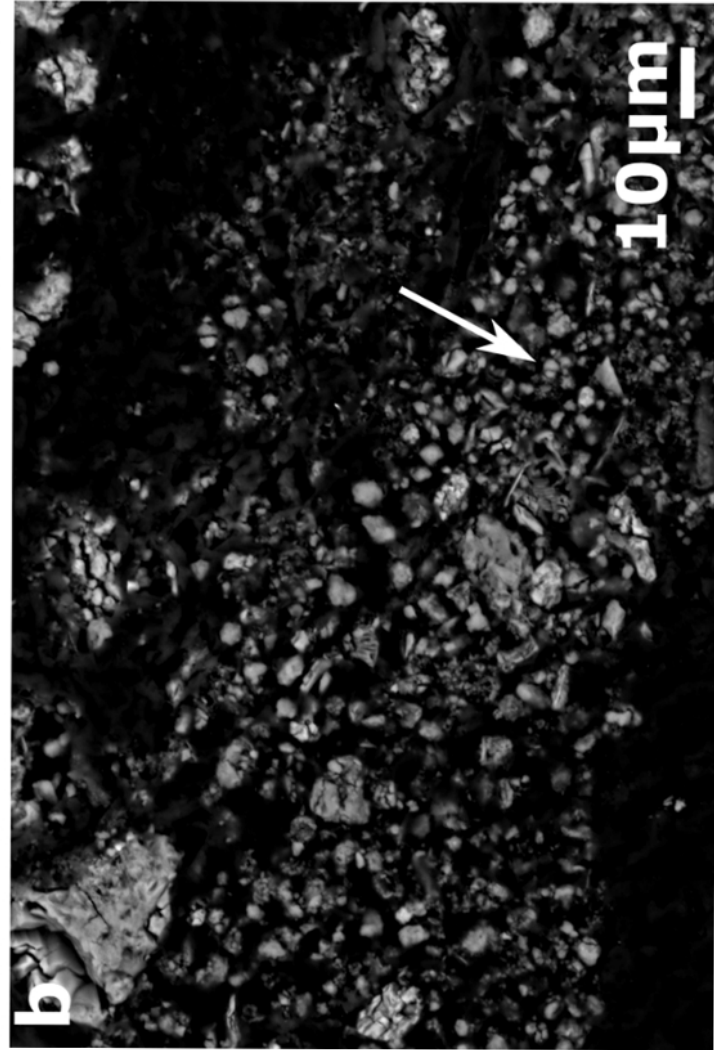
Figure 5

Figure 6

a) Microbial-mediated As cycling b) As immobilization in the EPS c) As preservation in CaCO$_3$ d) EPS is replaced by micrite

○ As(III)   ● As(V)   ✕ Ca   ▨ Carbonate   ◌ EPS